# 1D-to-2D tunneling in electron waveguides

Cristopher C. Eugster and Jesús A. del Alamo
*Massachusetts Institute of Technology, Cambridge, Massachusetts 02139*

Michael R. Melloch
*Purdue University, West Lafayette, Indiana 47907*

Michael J. Rooks
*National Nanofabrication Facility, Cornell University, Ithaca, New York 14853-5403*
(Received 2 June 1993)

We present a comprehensive experimental study of the tunneling and transport characteristics of split-gate "leaky" one-dimensional (1D) electron waveguides implemented in $Al_xGa_{1-x}As/GaAs$ heterostructures. In a leaky electron waveguide, electrons can tunnel out of the 1D channel through a thin side wall barrier into an adjacent 2D electron bath. A sharp peak and valley structure is observed in the 1D-to-2D tunneling current as the carrier concentration is modulated in the 1D waveguide through the field-effect action of the split gates. A semiclassical model confirms that the tunneling features originate from the 1D subbands in the channel.

## I. INTRODUCTION

Over the past decade, there has been much interest in understanding the physics behind transport in one-dimensional (1D) electronic systems.[1] A particularly intriguing 1D transport regime is that of an electron waveguide, in which, due to the absence of scattering in the channel, the electron behavior is solely determined by the confining potential. This new regime for electron device operation was first discovered by van Wees *et al.*[2] and Wharam *et al.*[3] in 1988. In their experiments, the individual modes of the electron waveguide were revealed by observation of quantized conductance as the width of the electron channel was modulated. Since then, other theoretical and experimental contributions have helped further clarify the physics behind 1D electron waveguiding.[4–10]

An independent experimental observation of the discrete propagation modes of an electron waveguide was recently provided in a tunneling spectroscopy experiment.[11] In these studies, we implemented a unique electron waveguide which had only a thin confining wall as one of its side barriers. Electrons traveling in the waveguide could tunnel out of the 1D channel through the thin sidewall into an adjacent two-dimensional (2D) electron bath. The tunneling current in these "leaky waveguides" showed very strong oscillations as the 1D carrier density was varied. The oscillatory structure was attributed to the sharp nature of the density of states (DOS) of the 1D electronic system.[11,12]

In this paper, we present a comprehensive study of the 1D-to-2D tunneling process in leaky electron waveguides. New experimental work carried out on entirely different samples has confirmed our original findings,[11] the strong peak and valley structure in the tunneling current. We have examined the dependence of the tunneling current on bias conditions and measurement temperature. In this paper, we also present a semiclassical theory for the tunneling phenomena which includes the length dependence of the waveguide and the energy dependence of the tunneling probability through the thin barrier. Numerical calculations confirm, to the first order, our experimental observations.

## II. THEORY

A leaky electron waveguide is much like a conventional electron waveguide studied in previous work[2,3,8] in that both have discrete modes, or subbands, which arise from the lateral confining potential. The unique feature of a leaky electron waveguide is a thin sidewall through which forward traveling electrons can tunnel out of the channel into an adjacent 2D electron bath. A conceptual illustration of the potential landscape of a leaky electron waveguide is shown in Fig. 1. In our scheme, we independently and simultaneously monitor the forward

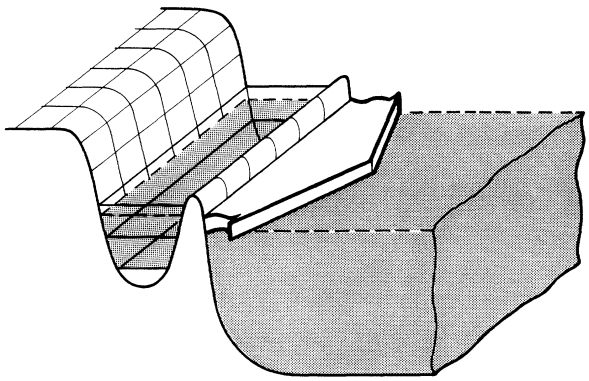

FIG. 1. Conceptual picture of the potential landscape of the leaky electron waveguide. Three 1D subbands are shown (two of which are occupied as illustrated by the shading). The arrow depicts the tunneling current through the thin middle barrier.

 

waveguide current and the leakage current tunneling into the 2D electron bath. In the limit of small leakage, the waveguide current is quantized due to the energy cancellation between the 1D density of states and the electron forward velocity. For the leakage current there is no similar energy cancellation since the transverse electron velocity is constant for a given subband. Therefore, the tunneling current largely reflects the features in the 1D density of states. This very simplified picture was advanced in our first presentation of this work,[11] and is shown in Fig. 2. In this section, we present a more rigorous model for the tunneling current $I_{S2}$ and the forward waveguide current $I_{S1}$.

In order to gain an intuitive understanding of the tunneling process, we use a semiclassical model to derive an expression for the tunneling current. In our picture, electrons bounce back and forth between the two sidewalls as they travel through the 1D channel. Each time they are incident on the thin sidewall, there is a finite probability that the electrons will tunnel through the barrier into the 2D electron bath. By assuming a uniform barrier along the waveguide and a small leakage current leaving the channel, the transverse problem can be isolated from the longitudinal one. The leaky waveguide cross section which is considered in our theory is shown in Fig. 3.

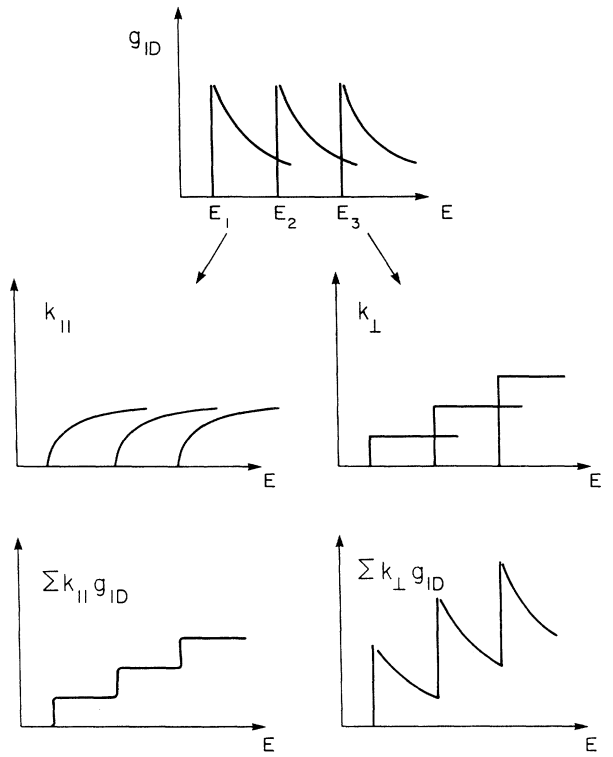


FIG. 2. Conceptual explanation for leaky waveguide characteristics. The left and right branches illustrate, respectively, the origin of the quantized conductance and the tunneling oscillations. Shown are the 1D density of states (top figure), the momentum components for the waveguide current (left branch) and the tunneling current (right branch), as well as the product of the momentum and density of states for the two branches.

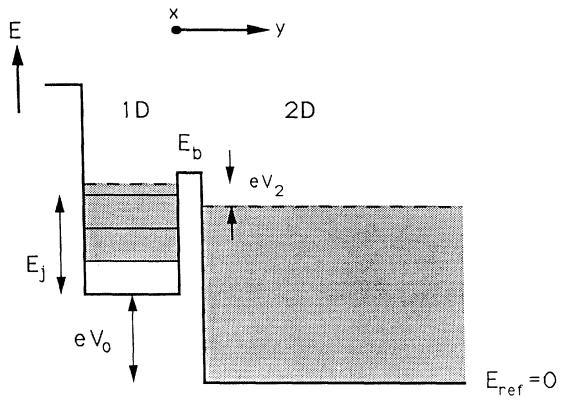


FIG. 3. Energy cross section of the ideal leaky electron waveguide. $E_j$ is the energy at the bottom of the $j$th subband, $eV_0$ is the increase in potential energy in the channel arising from the gate bias, $E_b$ is the energy at the top of the barrier, and $eV_2$ is the splitting between the Fermi levels.

We begin by outlining the rules in the tunneling process to show that the tunneling current is limited by the 1D side. Conservation of momentum requires that the $x$ and $z$ momentum components $k_x$ and $k_z$ remain the same during the tunneling process since the leakage current is flowing in the $y$ direction. The $z$ momentum component is automatically conserved since electrons on both sides of the barrier are in the lowest 2D subband. Momentum conservation in the $x$ direction requires that

$$k_{x2D}=k_{x1D}\ , \tag{1}$$

where the 1D and 2D subscripts denote the respective electronic systems on either side of the thin barrier. Energy conservation states (see Fig. 3)

$$eV_0+E_j+\frac{\hbar^2k_{x1D}^2}{2m^*}=\frac{\hbar^2k_{y2D}^2}{2m^*}+\frac{\hbar^2k_{x2D}^2}{2m^*}\ , \tag{2}$$

where $V_0$ is the potential difference between the two sides, $E_j$ is the increase in potential energy due to 1D quantization ($j$ is the 1D subband index), and $k_{y2D}$ is the $y$ momentum component on the 2D side. Since $k_x$ is conserved in the tunneling process, the $y$ momentum component on the 2D side can be found from Eq. (2),

$$k_{y2D}=\left[\frac{2m^*[E_j+eV_0]}{\hbar^2}\right]^{1/2}\ . \tag{3}$$

As seen by these selection rules, the momentum of the tunneling electrons are restricted by the 1D side.

In general, the tunneling current can be separated into two components: one arising from electrons tunneling from the 1D side to the 2D side, and the other resulting from electrons tunneling from the 2D side to the 1D side.

The 1D-to-2D tunneling component is calculated by multiplying the electron flux impinging on the thin barrier by the tunneling probability through the barrier. The flux is simply the rate of electron incidence on the thin sidewall times the number of electrons impinging at that rate. The rate can be arrived at by dividing the

transverse velocity by twice the waveguide width $w$:

$$R_j=\frac{\hbar k_{yj}}{m_* 2w} , \tag{4}$$

where $k_{yj}$ is the transverse momentum component, determined by $E_j$. The number of states in which electrons can occupy the 1D channel (for a particular subband) is given by the familiar density of states expression

$$g_{1D}dE=\frac{2}{\pi}dk_{x1D}. \tag{5}$$

An expression for the 1D-to-2D tunneling component per unit length, including contributions from all subbands $j$, can now be written as

$$J_{1D-2D}=e\sum_j R_j T_{1D-2D}\int_{-\infty}^{+\infty} g_{1D}(E-E_j-eV_0)f(E) \times[1-f(E+eV_2)]dE , \tag{6}$$

where $R_j$ is the impingement rate in Eq. (4), $T_{1D-2D}$ is the tunneling probability through the thin barrier,[13] and the 1D density-of-states integral gives the number of electrons in a given subband which are allowed to tunnel over to the 2D side. The $f(E)$ and $[1-f(E+eV_2)]$ terms determine the occupancy and availability of states on either side of the barrier, respectively. $eV_2$ is the splitting between the Fermi levels across the barrier.

The 2D-to-1D tunneling component can be arrived at in a similar fashion. As seen by the selection rules in Eqs. (1)–(3), the 1D side determines the number of electrons on the 2D side which can partake in the tunneling process. A general expression for the 2D-to-1D component is

$$J_{2D\text{-}1D}=e\sum_j R_{2D}T_{2D\text{-}1D}\int_{-\infty}^{+\infty} g_{1D}(E-E_j-eV_0) \times[1-f(E)]f(E+eV_2)dE , \tag{7}$$

where the 1D density of states expression in Eq. (5) is substituted for $dk_{x2D}$ in the above integral (remember that $k_{x2D}$ equals $k_{x1D}$). The impingement rate $R_{2D}$ and the 2D-to-1D tunneling probability $T_{2D\text{-}1D}$, are more complicated than the equivalent expressions in the 1D-to-2D tunneling component. However, the rate at which electrons enter the 1D side from the 2D side has to be equal to the rate at which electrons exit the 1D waveguide, since when $V_2=0$, the integrals in Eqs. (6) and (7) are identical. Therefore,

$$R_{2D}T_{2D\text{-}1D}=R_j T_{1D\text{-}2D} . \tag{8}$$

This allows us to arrive at the general expression for the tunneling current per unit length:

$$J_{S2}=J_{1D\text{-}2D}-J_{2D\text{-}1D} =e\sum_j R_j T_{1D\text{-}2D}\int_{-\infty}^{+\infty} g_{1D}(E-E_j-eV_0) \times[f(E)-f(E+eV_2)]dE . \tag{9}$$

The length dependence can be included by integrating along the $x$ direction of the waveguide. In the limit of small current, the tunneling current is

$$I_{S2}=el\sum_j R_j T_{1D\text{-}2D}\int_{-\infty}^{+\infty} g_{1D}(E-E_j-eV_0) \times[f(E)-f(E+eV_2)]dE , \tag{10}$$

where $l$ is the length of the waveguide. At low temperatures and for small Fermi-level splitting $eV_2$, $I_{S2}$ simplifies to

$$I_{S2}=e^2V_2\frac{l}{2w}\sum_j \frac{\hbar k_{yj}}{m^*}T_{1D\text{-}2D}(E_b-E_j-eV_0) \times g_{1D}(E_F-E_j-eV_0) , \tag{11}$$

where $E_F$ refers to the Fermi levels on either side of the barrier since their difference is small in comparison to the energy scale of the problem. The number of tunneling electrons is given by the 1D density of states at the Fermi level $E_F$. In addition, we have substituted the expression in Eq. (4) for $R_j$ in Eq. (10), as well as explicitly shown the energy dependence of the tunneling in the parentheses ($E_b$ is the barrier height).

There are several energy dependences in Eq. (11). The strongest one arises from $g_{1D}$, which results in a peak and valley structure in the tunneling current when the subbands are swept through the Fermi level as the electron concentration is modulated by means of a side-gate bias. A peak in the tunneling current corresponds to a subband just passing through the Fermi level since the density of states is highest near the bottom of the subband. This peak and valley structure is repeated as additional subbands are brought through the Fermi level. Therefore, the features in the 1D-to-2D tunneling current arise from the density of states in the 1D channel (the right-hand branch in Fig. 2).

The tunneling probability $T_{1D\text{-}2D}$ in Eq. (11) also has an effect on the features in the tunneling current. $T_{1D\text{-}2D}$ is determined by the barrier height with respect to the energy at the bottom of the subband since only the transverse electron wave function penetrates through the barrier. For a given subband at a certain bias, all electrons in the subband have the same tunneling probability, independent of energy $E$. For this reason, the transmission coefficient $T$ is outside the integral in all the above equations. As a subband passes below the Fermi level, its tunneling contribution diminishes as $E_b-E_j-eV_0$ increases, even more rapidly than the 1D density of states falloff. The tunneling current is thus primarily a result of electrons in the occupied subband nearest the Fermi level.

Equation (11) predicts a width dependence of the tunneling current through the $w$ and $k_{yj}$ terms. In split-gate schemes, the side-gate bias modulates both the width and the potential energy in the channel.[14] Under the hypothetical case where only the width is modulated ($eV_0=0$), $k_{yj}$ and $w$ change continuously with side-gate voltage ($k_{yj}$ is assumed to be inversely proportional to waveguide width $w$ for a given subband). The value of $k_{yj}$ at the Fermi level where tunneling dominates will be the same as when other subbands cross the Fermi level since the bottom of the channel does not change relative

to $E_F$. For this case, the height of the peaks predicted by Eq. (11) will have an inverse width relation. Under the other hypothetical case where only the potential energy is modulated, the values of $k_{yj}$ and $w$ will remain constant as the subbands sweep through the Fermi level. Here, the peak heights will be weighted by the different values of $k_{yj}$. In real experiments, the relative peak heights will be dependent on both a varying width and a changing potential energy in the channel.

The forward waveguide current $I_{S1}$ can be calculated in the usual manner found in the literature.[15] The small tunneling current leaking from the side of the waveguide is treated as a perturbation to transport in the channel. To first order, it is accounted for by simply subtracting $I_{S2}$ from the ideal value of the forward current in the following manner:

$$I_{S1}=e\sum_j\int_{-\infty}^{\infty}v_x(E-E_j-eV_0)\tfrac{1}{2}g_{1D}(E-E_j-eV_0)\times[f(E)-f(E+eV_1)]dE-I_{S2}\ , \quad (12)$$

where $v_x(E-E_j-eV_0)$ is the electron velocity in the forward direction for the $j$th subband, and $V_1$ is the applied voltage across the waveguide ($V_1=V_2$ in most of our experiments). The factor of $\frac{1}{2}$ before the 1D density-of-states term arises since we are interested only in those electrons moving in the positive $x$ direction. In the limit of low temperature and small $V_1$, the forward waveguide current becomes

$$I_{S1}=\frac{2e^2}{h}V_1\sum_j j-I_{S2}\ , \quad (13)$$

where $j$ is the subband index. The peaks in the tunneling current should occur ideally at the onset of a conductance step since this is when a new subband crosses the Fermi level. For large tunneling currents, the subtraction in Eq. (13) causes a rounding in the steps in the waveguide current, as seen in experiments.[11]

This section has put forward a simple semiclassical model for the tunneling current and the waveguide current in a leaky electron waveguide. We have shown that the tunneling current should have an oscillatory structure arising from the 1D subbands in the electron waveguide. We have also shown that the forward waveguide current is affected by the tunneling current. Other theoretical work involving complete quantum-mechanical solutions is consistent with our semiclassical picture of leaky electron waveguide devices.[12,16,17]

## III. DEVICE FABRICATION

Our work is based around a split-gate[18,19] dual electron waveguide device,[20] sketched in Fig. 4, with the ultimate goal of exploring electron directional coupling between two 1D electron waveguides.[21] Such a device consists of three gates patterned on top of a depletion-mode modulation-doped heterostructure. By applying a negative bias to these gates, we can deplete the 2D electron gas (2DEG) at the heterointerface forming the two closely spaced 1D electron waveguides. The two side-gate biases control the carrier concentration in each respective waveguide. The middle-gate bias establishes the thin tunneling barrier between the two 1D waveguides.

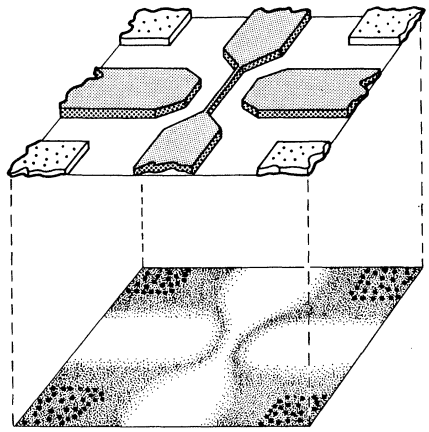

FIG. 4. Conceptual picture of dual electron waveguide device. The top plane shows the gates and Ohmic contacts at the surface of the heterostructure. The bottom plane shows electron concentration (shaded regions) at the heterointerface for negative gate biases.

In this paper, we are interested only in tunneling between a 1D electron waveguide and a 2D electron bath. This single leaky electron waveguide can be implemented by grounding one of the side gates of our dual electron waveguide structure. This leaves the 2DEG underneath that gate unaffected and therefore establishes a waveguide with a 2DEG next to it, separated by a thin barrier of controllable strength.

Two heterostructures were used for the measurements reported in this paper. They are shown in Figs. 5(a) and 5(b). The main difference between them is the size of the spacer region separating the dopants from the 2DEG. For the shallow heterostructure (used in Ref. 11), shown in Fig. 5(a), which has the smaller spacer, the 2DEG mobility is 170 000 $cm^{-2}/V\,s$, and the 2D carrier concentration is $7\times10^{11}$ $cm^{-2}$ at $T=4.2$ K. The deep heterostructure, shown in Fig. 5(b), has a 2DEG mobility of $1.2\times10^6$ $cm^2/V\,s$, and a 2D carrier concentration of $4\times10^{11}$ $cm^{-2}$ at $T=4.2$ K. The values for the deep heterostructure have been optimized for both high mobility and high carrier concentration using a multilayer $\delta$-doping growth technique.[22] Both are necessary for good electron waveguiding.[8]

We expect cleaner waveguides characteristics in the deep heterostructure than in the shallow heterostructure because of its higher mobility. However, since the 2DEG is much further away from the split gates in the deep heterostructure (890 vs 525 Å), the confining potentials will be softer, resulting in smaller subband separations and wider tunneling barriers. In Sec. V, we will see the effects of this on the features of the waveguide and tunneling currents.

Device fabrication after heterostructure growth proceeds with optical lithography for mesa isolation, Ohmic contacts, and gate pads. The fine split gates are then fabricated using direct-write electron-beam lithogra-

phy. If necessary, an additional gate metal is deposited using optical lithography to ensure continuity between the fine split-gate metal and the gate pads. Figure 6 shows a scanning electron micrograph (SEM) faraway view of a finished device.

The mesas are formed by wet etch using a 10:1 $H_2O$/etchant solution where the etchant is $[H_2SO_4]:[H_2O_2]:[H_2O]$ (1:10:10). The Ohmic contacts are formed by *e* beam evaporating a Ni/Au/Ge multilayer (5 nm of Ni, 5 nm of Au, 25 nm of Ge, 45 nm of Au, 10 nm of Ni, and 50 nm of Au) followed by a 425 °C, 10-s rapid thermal anneal. Four Ohmic contacts are fabricated for each device to allow individual access to the two waveguides. The gate pads are fabricated by *e* beam evaporating a Ti/Au bilayer before (20 nm of Ti and 100 nm of Au) and after (30 nm of Ti and 300 nm of Au) the fine split-gate lithography.

(a)

| | |
|---|---|
| GaAs | 50 Å |
| n-AlGaAs $10^{18}$ cm$^{-3}$ | 400 Å |
| i-AlGaAs | 55 Å |
| AlAs | 20 Å |
| i-GaAs | 1.0 um |
| undoped-GaAs substrate | |

(b)

| | |
|---|---|
| n-GaAs $\sim 10^{18}$ cm$^{-3}$ | 50 Å |
| δ-doped $Al_{0.3}Ga_{0.7}As$ $4\times10^{11}$ cm$^{-2}$ | 600 Å |
| (Silicon atoms in planes every 40 Å) | |
| i-$Al_{0.3}Ga_{0.7}As$ | 240 Å |
| i-GaAs | 1 μm |
| LTBL (GaAs Buffer Layer Grown at a Substrate Temperature of 250°C) | 1 μm |
| i-GaAs | 1 μm |
| Undoped GaAs substrate | |

FIG. 5. Cross sections of (a) the shallow heterostructure, and (b) the deep heterostructure.

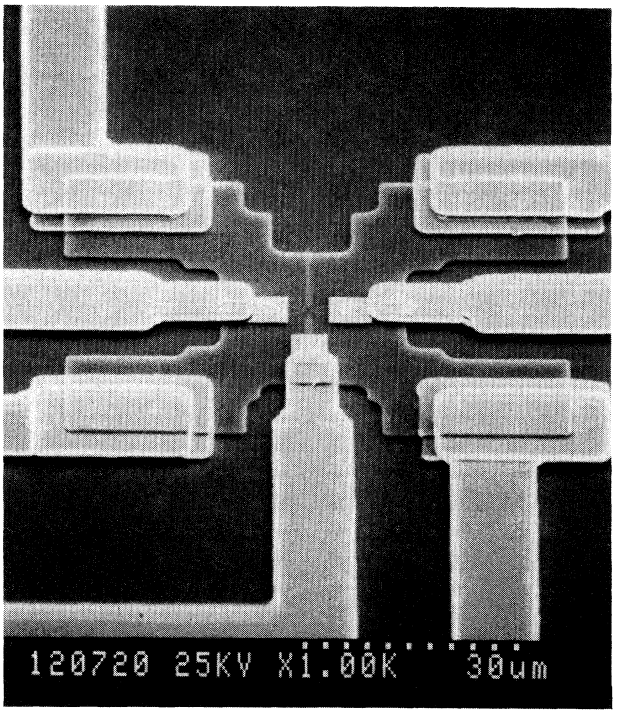


FIG. 6. Scanning electron micrograph (SEM) of the complete device including mesa, Ohmic contacts, gate pads, and fine split gates.

A typical electron-beam-written gate pattern is shown from a distant and close-up view in Figs. 7(a) and 7(b), respectively. The electron-beam lithography uses a bilayer poly(methylmethacrylate) (PMMA) technique to achieve high yield lift-off.[23] The thermally evaporated metal in the *e*-beam lithography process is a 20-nm Au/Pd alloy which has a very small grain size. The common middle gate used to create the leaky barrier is fabricated using a single-pass *e*-beam lithography technique.[23] Its width is approximately 30 nm. In order to achieve such small feature size, proximity effects have to be reduced; therefore, only the periphery of the side gates are drawn. This does not compromise input/output isolation.[24] The middle gate is widened to 0.5 $\mu$m in the areas outside the waveguide region in order to provide isolation between the 2D electron baths. We fabricated several devices with various lithographic dimensions: $W$ is the distance between the side gates and the middle gate, and $L$ is the length of the central region of the split gates.

For the shallow heterostructure, the sheet resistances, as measured by the transmission line method (TLM) technique, are 1200 and 55 Ω/□ at 300 and 4.2 K, respectively. The contact resistance is 0.27 Ω mm at 4.2 K. For the deep heterostructure, the sheet resistance is 1700 Ω/□, and the contact resistance is 0.3 Ω mm at 300 K.

## IV. DEVICE BIAS CONDITIONS

In order to maintain consistency with our previous papers, the two electron waveguide in our device are re-

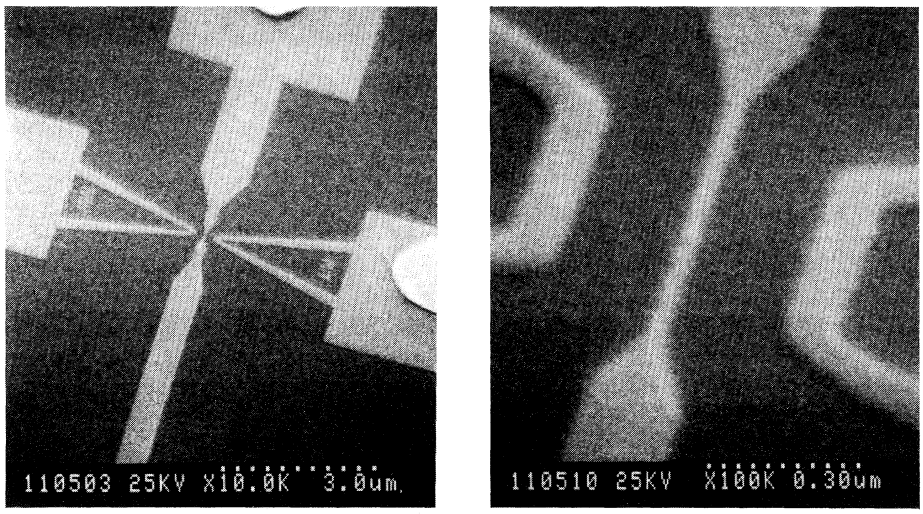


FIG. 7. SEM distant and close-up views of the split gates used to implement the leaky electron waveguide. The middle gate, which serves as the tunneling barrier for the channel, is 30 nm wide.

ferred to as the "top waveguide" and "bottom waveguide." The side gates associated with the respective waveguides are then labeled "top gate" and "bottom gate." The thin common gate to both waveguides is referred to as "middle gate".

In our measurements, one of the side-gate biases [either the top-gate voltage ($V_{GT}$) or the bottom-gate voltage ($V_{GB}$)] is swept depending on which electron waveguide is being studied. The middle gate is fixed at a negative bias which allows only a small tunneling current to pass through the thin barrier in the central portion of the device while providing good isolation in the outer regions of the device. This arises from short-channel effects, since the middle gate is lithographically wider in the outer regions.[20] The remaining side gate is grounded so a 2D electron bath exists on the other side of the thin waveguide sidewall. The bias schematics for implementing a top "leaky" electron waveguide and a bottom "leaky" electron waveguide are shown respectively in Figs. 8(a) and 8(b).

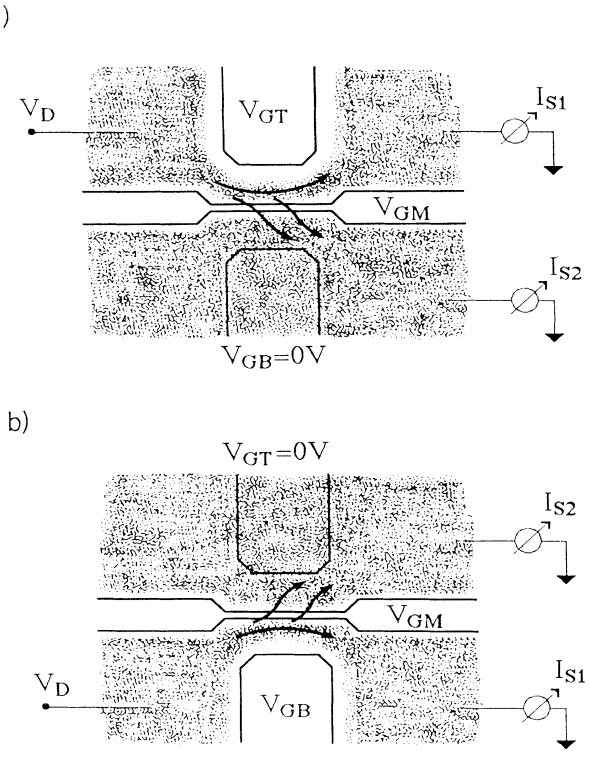


FIG. 8. Bias conditions for (a) a top leaky electron waveguide, and (b) a bottom leaky electron waveguide. The shaded regions indicate the electron-gas distribution at the heterointerface.

A small ac ($f=19$ Hz) voltage is applied between the drain and source contacts of the waveguide. This voltage is referred to as $V_{DS1}$ (in the absence of any series resistance, equal to $V_1$ in our theory). The source current flowing through the waveguide, referred to as $I_{S1}$, is fed into a current-to-voltage preamplifier whose output is monitored by a lock-in amplifier. The 2DEG on the other side of the thin middle gate is also contacted and kept at the same potential as the waveguide source contact, as illustrated in Fig. 8. The voltage between the drain contact and this contact is referred to as $V_{DS2}$ (in the absence of series resistance, equal to $V_2$ in our theory). Since $V_{DS1}$ is equal to $V_{DS2}$ in our experiments, from now on we will drop the numerical subscript and refer only to the drain-source voltage as $V_{DS}$. The current flowing out of the 2DEG contact is the tunneling current, referred to as $I_{S2}$, and it is monitored by a different preamplifier–lock-in setup. In general, the tunneling current $I_{S2}$ is much smaller in magnitude than the waveguide current $I_{S1}$. All measurements are carried out at $T=1.6$ K and $V_{DS}=100\ \mu$V unless otherwise specified.

## V. EXPERIMENTAL RESULTS

The $I_S$-$V_{GT}$ characteristics of an $L=1.0\ \mu$m, $W=0.3\ \mu$m leaky electron waveguide implemented in the deep heterostructure are shown in Fig. 9. The forward

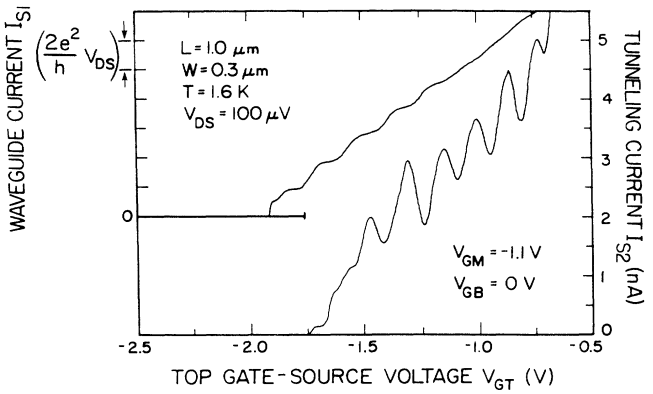


FIG. 9. Top leaky waveguide $I_S$-$V_{GT}$ characteristics showing the current $I_{S1}$ flowing through the waveguide, and the tunneling current $I_{S2}$ leaking out of the channel through the thin sidewall barrier. This device was implemented in the deep heterostructure.

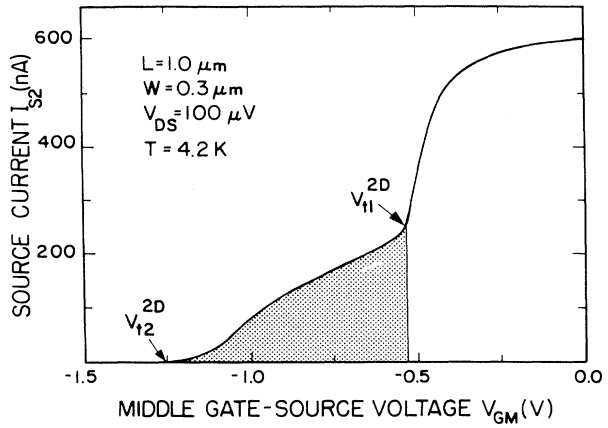


FIG. 10. Middle-gate $I_{S2}$-$V_{GM}$ characteristics for a device implemented in the deep heterostructure ($V_{GT}=V_{GB}=0$ V). The threshold voltages for the 2D electron gas underneath the wide and narrow portions of the middle gate are labeled $V_{t1}^{2D}$ and $V_{t2}^{2D}$, respectively.

waveguide current $I_{S1}$ shows sharp steps of magnitude $(2e^2/h)V_{DS}$ as the top-gate bias sweeps the subbands through the Fermi level. The first five steps are especially clean while the higher-lying ones are somewhat less visible. This indicates the presence of nonuniformities in the confining potential near the side gate, which is verified by an asymmetric bias technique.[25–27] The tunneling current $I_{S2}$ shows the theoretically predicted peak and valley structure arising from the 1D subbands, consistent with our previous experimental findings.[11] Ideally a new peak should occur at the onset of a new step since this corresponds to a subband crossing through the Fermi level. Except for the first two subbands, the expected line up is observed in Fig. 9. The tunneling current $I_{S2}$ becomes zero when $I_{S1}=0$, which confirms that tunneling only occurs in the middle central region of the device.

An independent confirmation of the 2DEG isolation in the outer device regions can be obtained by directly measuring the middle-gate characteristics with the side gates grounded. The resulting $I_S$-$V_{GM}$ characteristics are shown in Fig. 10. Two thresholds are noted, one in which the 2DEG is turned off underneath the wider portions of the middle gate, $V_{t1}^{2D}\sim -0.6$ V, and another in which the electron gas is turned off underneath the narrow portion of the middle-gate, $V_{t2}^{2D}\sim -1.2$ V. The value of $V_{t2}^{2D}$ is sensitive to the exact dimensions of the middle gate. By biasing the middle gate beyond the first threshold $V_{t1}^{2D}$, the outer 2DEG regions become completely isolated from one another. In our tunneling experiments, we bias the middle gate in a tunneling regime near $V_{t2}^{2D}$.

We note that the tunneling current is not affected when the 2D electron concentration is modulated on the other side of the barrier. Figure 11 shows the tunneling characteristics for an $L=0.5$ μm, $W=0.3$ μm bottom leaky waveguide under different fixed top-gate biases (while still maintaining a 2DEG underneath the top gate). Both the features and the magnitude of the current $I_{S2}$ are independent of the changes in carrier concentration on the 2D side. This confirms our theory which postulates that the tunneling current is limited by the 1D side.

The higher mobility, deep heterostructure has led to an overall improvement in conductance quantization as well as in waveguide yield over our previous work.[11] Almost all of the devices measured showed some degree of quantization in the waveguide current as well as observable oscillations in the tunneling current. That was not the case for the shallow heterostructure. We were therefore able to find a few devices in which both waveguides were relatively free of scatterers. Figure 12 shows the tunneling current $I_{S2}$ for the top leaky waveguide and the bottom leaky waveguide of a single $L=0.2$ μm, $W=0.3$ μm device. The nearly identical characteristics of both waveguides help confirm that the observed features arise from the potential landscape imposed by the symmetric gate pattern, and not by an arbitrary impurity configuration.

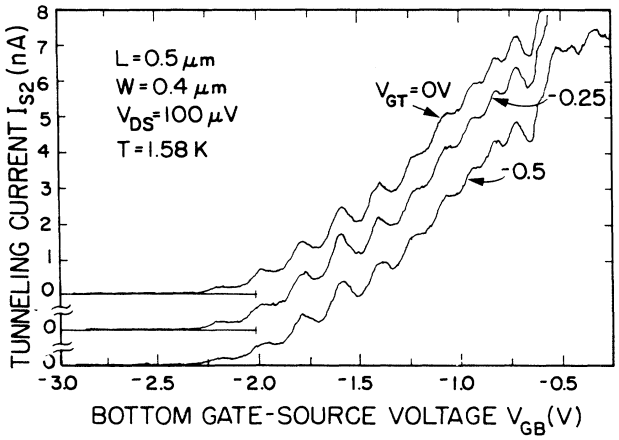


FIG. 11. Tunneling characteristics $I_{S2}$-$V_{GB}$ of the bottom leaky waveguide for different values of top-gate bias (deep heterostructure).

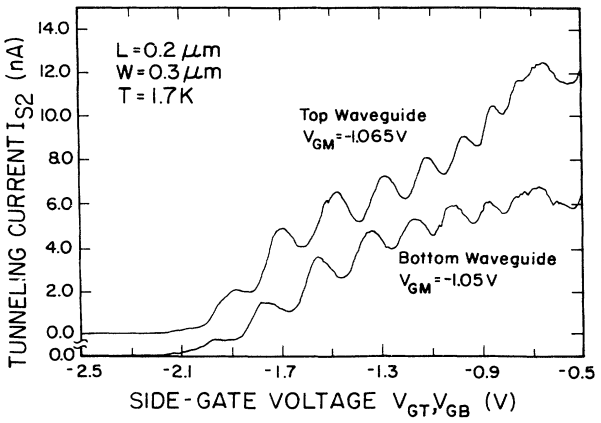


FIG. 12. The tunneling characteristics $I_{S2}$-$V_{(GT,GB)}$ of the top and bottom waveguides in an $L=0.2$ $\mu$m, $W=0.3$ $\mu$m device implemented in the deep heterostructure.

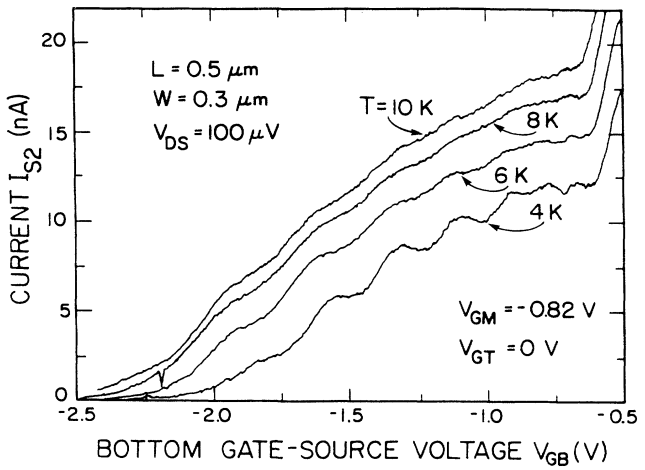


FIG. 14. Temperature dependence of the tunneling features for the bottom leaky waveguide (deep heterostructure).

We have found that the strength of the middle barrier affects the quality of the quantization in the waveguide current. Figure 13 shows the $I_S$-$V_{GT}$ characteristics for an $L=0.5$ $\mu$m, $W=0.3$ $\mu$m device biased in the leaky waveguide configuration for two different values of middle-gate bias, $V_{GM}=-1.2$ and $-1.15$ V. For the more positive middle-gate bias, there is more tunneling current out of the waveguide ($I_{S2}$ increases). At the same time, the staircase structure in $I_{S1}$ almost completely washes out, resulting from the weaker confinement. The reduction in the middle-gate bias has also led to a slightly wider waveguide, since the threshold for the 1D electron waveguide becomes more negative.

We also studied the temperature dependence of the tunneling current. Thermal broadening will smear the electron energies around the Fermi level by 3.5 kT.[15] Figure 14 shows the $I_{S2}$-$V_{GT}$ characteristics of an $L=0.5$ $\mu$m, $W=0.3$ $\mu$m device implemented in the deep heterostructure for temperatures from $T=4.2$ to 10 K. The oscillations are noted to wash out around 10 K, which corresponds to a 3.5-kT value of 3 meV, close to the calculated energy-level separations in split-gate-defined channels.[14,28] The peak and valley structure of the tunneling current is expected to smear together when this energy value approaches the subband separation. In addition, there is an overall increase in $I_{S2}$ for higher temperatures in Fig. 14. This is a result of a substantial thermionic emission component over the thin middle barrier, riding on top of the tunneling current.

The impact of temperature cycling on the features of the leaky electron waveguides was also investigated. Figure 15 shows the $I_S$-$V_{GT}$ characteristics of an $L=0.1$ $\mu$m, $W=0.2$ $\mu$m device implemented in the shallow heterostructure, both before and after cycling up to room temperature. The general features are largely unperturbed following thermal cycling, which implies that the peak and valley structure in the tunneling current results from the potential landscape imposed by the shape of the split gates and the voltage applied to them. There are

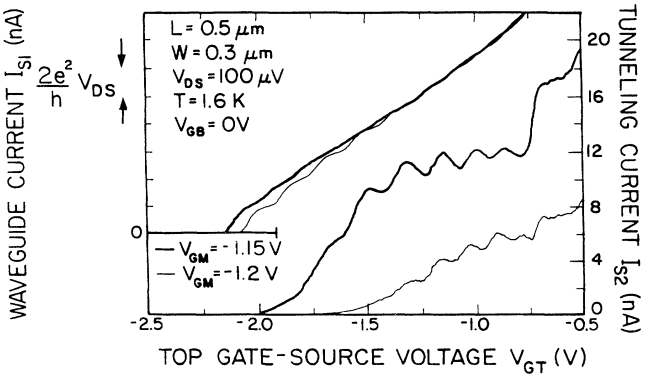


FIG. 13. Top leaky waveguide characteristics for different values of the middle-gate bias, $V_{GM}=-1.2$ and $-1.15$ V (deep heterostructure).

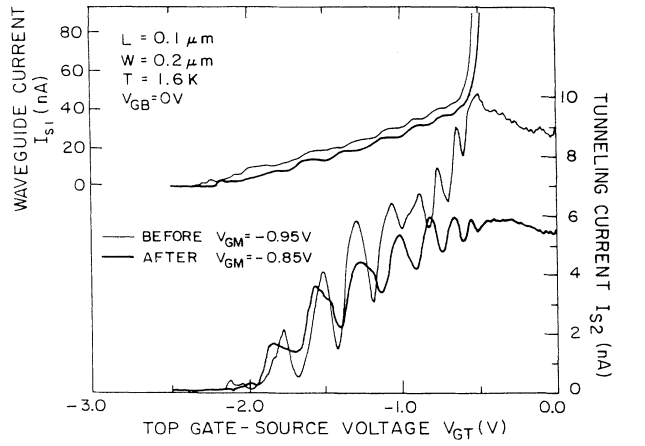


FIG. 15. Top leaky waveguide characteristics for the shallow heterostructure. Characteristics after temperature cycling up to $T=300$ K are also shown.

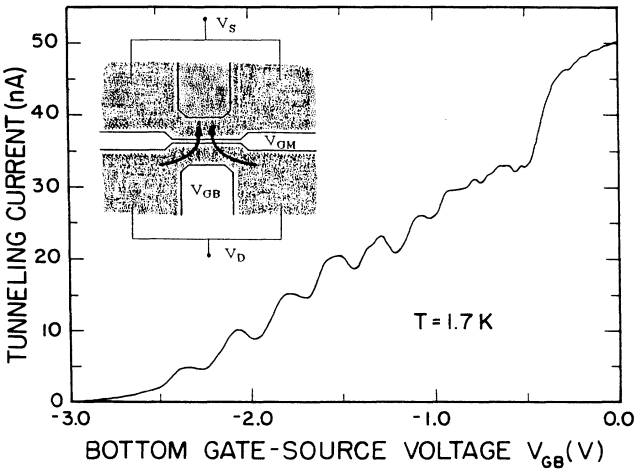


FIG. 16. Characteristics of an $L=0.5\ \mu$m, $W=0.25\ \mu$m bottom leaky waveguide under common drain and source bias configurations (see inset). $V_{DS}$ is equal to 100 $\mu$V ($V_{GM}=-0.9$ V and $V_{GT}=0$ V).

some noticeable changes in the details of the features which suggests that impurities are affecting the shape of the confining potential. The peak to valley ratio as well as the magnitude of the tunneling current decreases after temperature cycling, signifying a modified barrier. The threshold voltages of the middle and side gates are also noted to shift positive upon thermal cycling.

We also studied the case in which the voltage applied across the waveguide is brought to zero ($V_1=0$ V). For this bias condition, the lower contacts are tied together as drain and the upper contacts are tied together as source (see inset in Fig. 16). The results show the familiar peak and valley structure in the tunneling current illustrated in Fig. 16. This measurement is an important confirmation of our claims since the tunneling structure should not be dependent on the drain-source bias configuration. It should only be affected by the 1D density of states and the tunneling probability.

The oscillatory features in the tunneling current are quite consistent between the two different heterostructures used in our experiments. The most noticeable difference between their characteristics is that the peak to valley ratios of the tunneling oscillations for the deep heterostructure are smaller than those observed for the shallow heterostructure.[11] We attribute this to the increased distance between the gates and the 1DEG which results in both smaller subband separations and a wider tunneling barrier. The smaller subband separations cause the features in the tunneling current to smear together. For a wider tunneling barrier, the height of the barrier must be reduced in order to measure similar tunneling current levels as through a thin barrier. This results in weaker waveguide confinement and increased thermionic emission current over the barrier.

## VI. SIMULATIONS

This section compares the experimental results with numerical predictions based on the theory presented in Sec. II. In order to carry out the simulations, we must first estimate the height of the tunneling barrier which, to first order, can be found from the temperature-dependence measurements. This is a measurement in which all the biases are fixed and only the temperature is varied. Therefore any changes in the current $I_{S2}$ will be a result of thermally activated processes and thermal smearing. In general, in addition to the tunneling component extensively discussed above, $I_{S2}$ will also contain a thermionic emission component of electrons over the barrier. By charting $I_{S2}$ versus 1/kT in an Arrhenius plot, the height of the barrier relative to the Fermi level can be extracted, to first order, from the slope of the line passing through the data points.

Figure 17 shows an Arrhenius plot for the valley current levels in Fig. 14. A clear thermally activated behavior is observed. The extracted values of the barrier height above $E_F$ lie in a range of 0.8–0.24 meV for the second through seventh valleys. The barrier height is noted to increase rapidly for the lower valleys. This is most likely a result of the weak modulation of the middle barrier by the side-gate bias near threshold. For high electron concentrations in the 1D channel, the electron gas effectively isolates the electrostatic action of the side

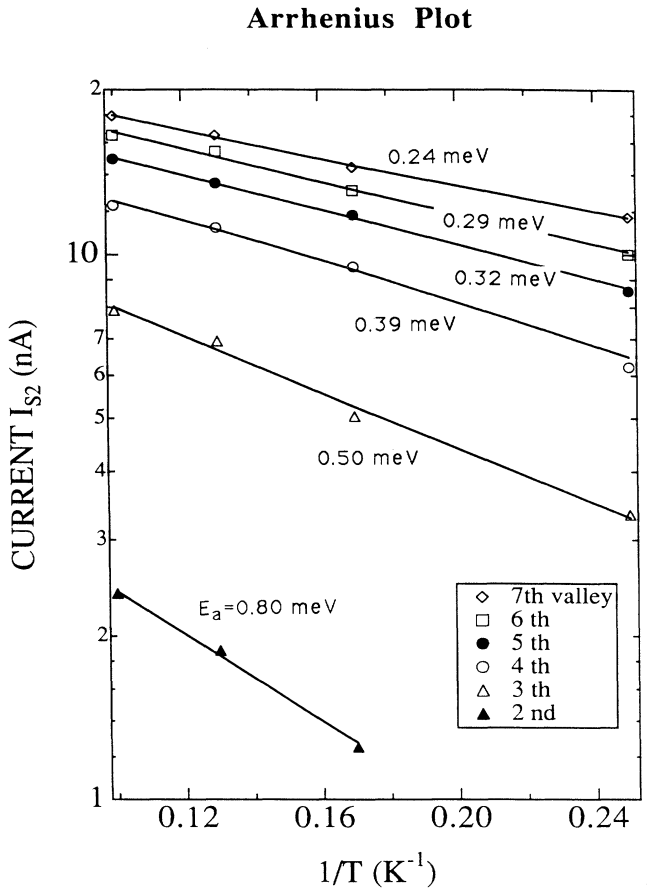


FIG. 17. Arrehnius plot of second through fifth valley levels of data in Fig. 14. The thermal activation energy $E_a$ for the different valleys range from 0.24 to 0.8 meV.

and middle gates. As the electron population in the 1D channel is reduced by means of the side-gate bias (this corresponds to lower-order valleys), the electron gas does not completely screen out the tails of the potential. As a result, the middle barrier is raised as the side gate sweeps negative. This finding explains why the peaks get higher as the side-gate bias sweeps positive. It also explains why in the deep heterostructure, it is very difficult to resolve tunneling from the first and second subbands.

For our simulations, we assume a constant energy subband spacing of 2 meV which does not change as the subbands are swept through the Fermi level. This scenario is most accurate for the first few subbands in which the potential in the waveguide is lifted with more negative side-gate bias. This assumption does not restrict the conclusions that are reached below. The barrier width is kept fixed at $d = 350$ Å in the simulations reported in this paper. The barrier height with respect to the Fermi level in the waveguide is varied continuously from 1 meV for the lowest subband to 0.3 meV for the fifth subband, roughly consistent with the values extracted from the Arrhenius plot. The transmission coefficient for the rectangular barrier used in the simulations can be found in Ref. 13.

The simulations were carried out for $T = 1.6$ K conditions. Thermal broadening is included in the simulations in the manner outlined by Bagwell and Orlando.[15] Voltage broadening is negligible in our experiments and does not affect the simulation results.

Figures 18(a) and 18(b) show the simulated tunneling current $I_{S2}$ and the simulated waveguide current $I_{S1}$, respectively, in a leaky electron waveguide device. The current values are consistent with those measured in the experiments. The tunneling features in Fig. 18(a) closely resemble those observed in our measurements. As expected from the theory, the steps in the forward waveguide current $I_{S1}$ in Fig. 18(b) line up with the individual oscillations in the tunneling current $I_{S2}$ in Fig. 18(a). Each new oscillation occurs at the onset of a new conductance step.

The simulations show that the tunneling features are rounded from thermal smearing. Simulations carried out for lower-temperature conditions show much sharper onsets. Our simulations also show that the tunneling features drop off faster than expected by the density of states. This again becomes much more evident at lower temperatures. Once the subbands pass far enough below the Fermi level, their tunneling component becomes negligible due to a rapidly diminishing tunneling probability.

In our simple picture, the tunneling current is directly subtracted from the waveguide current. When the tun-

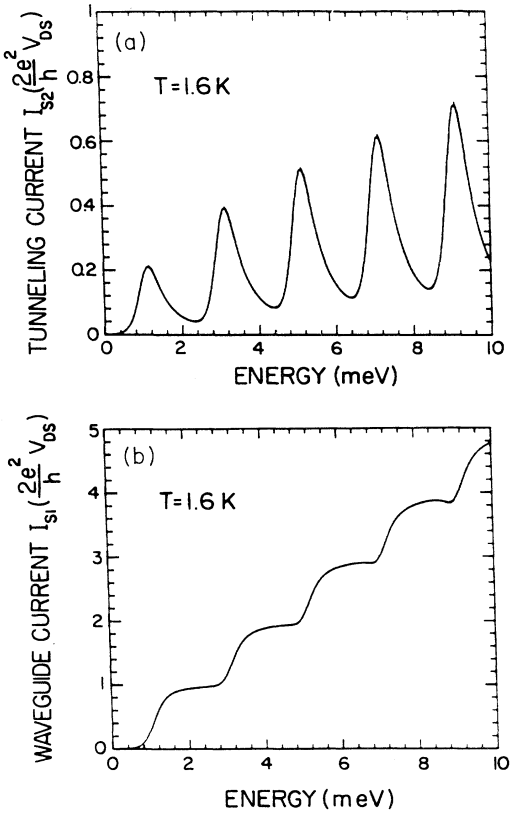


FIG. 18. Simulated (a) tunneling and (b) waveguide currents vs energy for a leaky waveguide device ($d = 350$ Å, $l = 0.5$ $\mu$m, and $w = 0.25$ $\mu$m). The barrier height with respect to the Fermi level is varied from 1 to 0.3 meV.

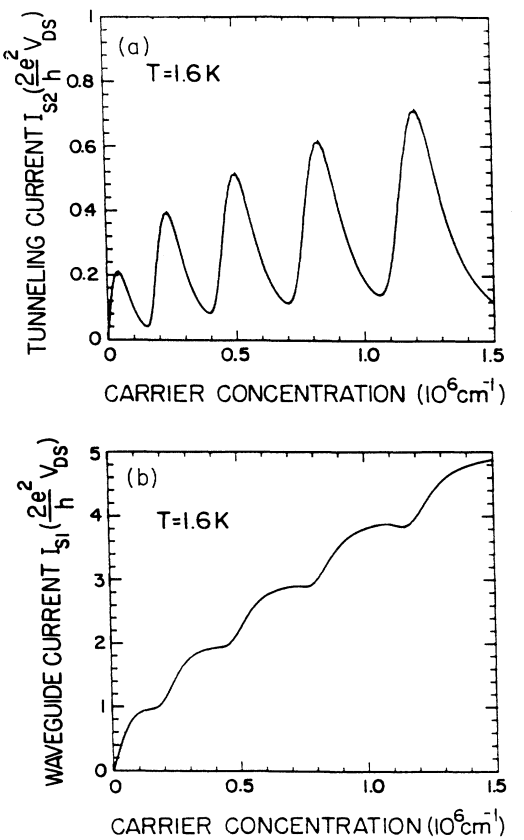


FIG. 19. Simulated (a) tunneling and (b) waveguide currents vs carrier concentration for a leaky waveguide device (same parameters as in Fig. 18).

neling current becomes large enough, a noticeable rounding of the quantized conductance steps occurs. In our experiments, we often see degradation in the quantized conductance as the tunneling current increases. Other factors, not accounted for in the simulations, also affect the quality of the quantized conductance in leaky waveguides, such as weak confinement and increased scattering along the barrier.

Figures 19(a) and 19(b) show simulated tunneling and waveguide currents, respectively, as a function of the carrier concentration in the 1D waveguide. The carrier concentration in the waveguide is related to the side-gate voltage through a weakly changing variable, namely the capacitance. Therefore, plotting $I_{S1}$ and $I_{S2}$ as functions of the carrier concentration provides a picture that more closely resembles experimental observations. The general features in Fig. 19 become more spread out, causing more symmetric tunneling oscillations with side-gate voltage. Such broadening is partly the cause of the finite smearing of the observed features in $I_{S1}$ and $I_{S2}$.

## VII. CONCLUSIONS

This paper has presented a comprehensive set of experiments of 1D-to-2D tunneling in leaky electron waveguides. In agreement with our previous findings,[11] the tunneling current from the side of a leaky waveguide shows a strong peak and valley structure as the 1D carrier concentration is modulated. The features in the tunneling current are shown to arise from the 1D subbands in the electron waveguide. Our work provides an experimental confirmation of electron waveguiding in a 1D electronic system which is completely independent of the observation of conductance quantization.

## ACKNOWLEDGMENTS

We would like to acknowledge helpful discussions with J. Smet, Q. Hu, and P. Bagwell. This work has been funded by NSF Contracts Nos. 87-19217-DMR, DMR-9022933, and 9157305-ECS. C.C.E. acknowledges support from IBM.

[1]C. W. J. Beenakker and H. van Houten, in *Solid State Physics, Semiconductor Heterostructures and Nanostructures,* edited by H. Ehrenreich and D. Turnbull (Academic, New York, 1991), p. 1.

[2]B. J. van Wees, H. van Houten, C. W. J. Beenakker, J. G. Williamson, L. P. Kouwenhoven, D. van der Marel, and C. T. Foxon, Phys. Rev. Lett. **60**, 848 (1988).

[3]D. A. Wharam, T. J. Thornton, R. Newbury, M. Pepper, H. Ahmed, J. E. F. Frost, D. G. Hasko, D. C. Peacock, D. A. Ritchie, and G. A. C. Jones, J. Phys. C **21**, L209 (1988).

[4]L. I. Glazman, G. B. Lesovik, D. E. Khmel'nitskii, and R. I. Shekhter, Pis'ma Zh. Eksp. Teor. Fiz. **48**, 218 (1988) [JETP Lett. **48**, 238 (1988)].

[5]A. Szafer and A. D. Stone, Phys. Rev. Lett. **62**, 300 (1989).

[6]M. Buttiker, Phys. Rev. B **41**, 7906 (1990).

[7]L. Escapa and N. Garcia, Appl. Phys. Lett. **56**, 901 (1990).

[8]G. Timp, R. Behringer, S. Sampere, J. E. Cunningham, and R. E. Howard, *Nanostructure Physics and Fabrication,* edited by M. A. Reed and W. P. Kirk (Academic, New York, 1989), p. 331.

[9]L. Kouwenhoven, B. van Wees, C. Harmans, J. Williamson, H. van Houten, C. Beenakker, C. Foxon, and J. Harris, Phys. Rev. B **39**, 8040 (1989).

[10]K. Ismail, S. Washburn, and K. Y. Lee, Appl. Phys. Lett. **59**, 1998 (1991).

[11]C. C. Eugster and J. A. del Alamo, Phys. Rev. Lett. **67**, 3586 (1991).

[12]Y. Takagaki and D. K. Ferry, Phys. Rev. B **45**, 12 152 (1992).

[13]A. P. French and E. F. Taylor, *An Introduction to Quantum Physics* (Norton, New York, 1978).

[14]S. E. Laux, D. J. Frank, and F. Stern, Surf. Sci. **196**, 101 (1988).

[15]P. F. Bagwell and T. P. Orlando, Phys. Rev. B **40**, 1456 (1989).

[16]P. F. Bagwell (private communication).

[17]E. Gornik, W. Demmerle, J. Smoliner, G. Bohm, and G. Weimann (unpublished).

[18]T. J. Thornton, M. Pepper, H. Ahmed, D. Andrews, and G. J. Davies, Phys. Rev. Lett. **56**, 1198 (1986).

[19]H. Z. Zheng, H. P. Wei, D. C. Tsui, and G. Weimann, Phys. Rev. B **34**, 5635 (1986).

[20]C. C. Eugster, J. A. del Alamo, M. J. Rooks, and M. R. Melloch, Appl. Phys. Lett. **60**, 642 (1992).

[21]J. A. del Alamo and C. C. Eugster, Appl. Phys. Lett. **56**, 78 (1990).

[22]M. R. Melloch, D. C. Miller, and B. Das, Appl. Phys. Lett. **54**, 943 (1989).

[23]M. J. Rooks, C. C. Eugster, J. A. del Alamo, G. L. Snider, and E. L. Hu, J. Vac. Sci. Technol. B **9**, 2856 (1991).

[24]C. C. Eugster, J. A. del Alamo, and M. J. Rooks, Jpn. J. Appl. Phys. **29**, L2257 (1990).

[25]G. Timp, R. E. Behringer, and J. E. Cunningham, Phys. Rev. B **42**, 9259 (1990).

[26]J. G. Williamson, C. E. Timmering, C. J. P. M. Harmans, J. J. Harris, and C. T. Foxon, Phys. Rev. B **42**, 7675 (1990).

[27]C. C. Eugster, J. A. del Alamo, M. R. Melloch, and M. J. Rooks, Phys. Rev. B **46**, 10 146 (1992).

[28]G. L. Snider, I.-H. Tan, and E. L. Hu, J. Appl. Phys. **68**, 5922 (1990).

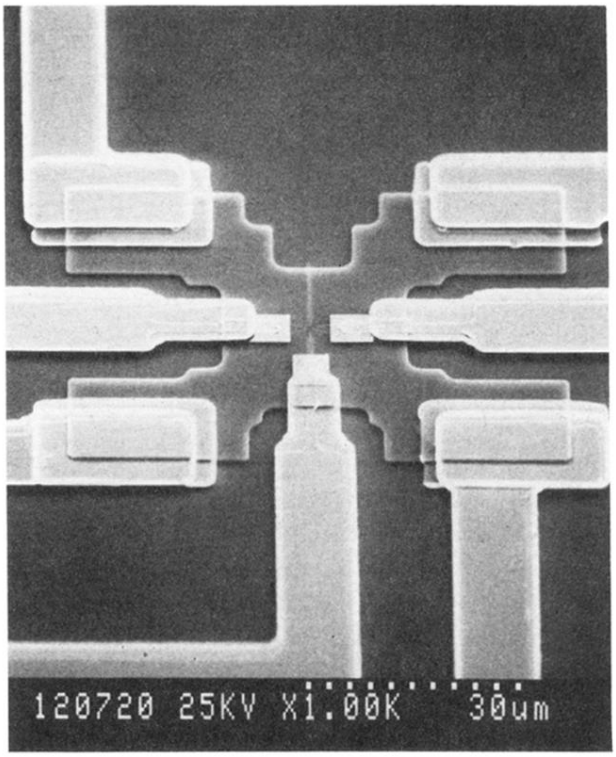


FIG. 6. Scanning electron micrograph (SEM) of the complete device including mesa, Ohmic contacts, gate pads, and fine split gates.

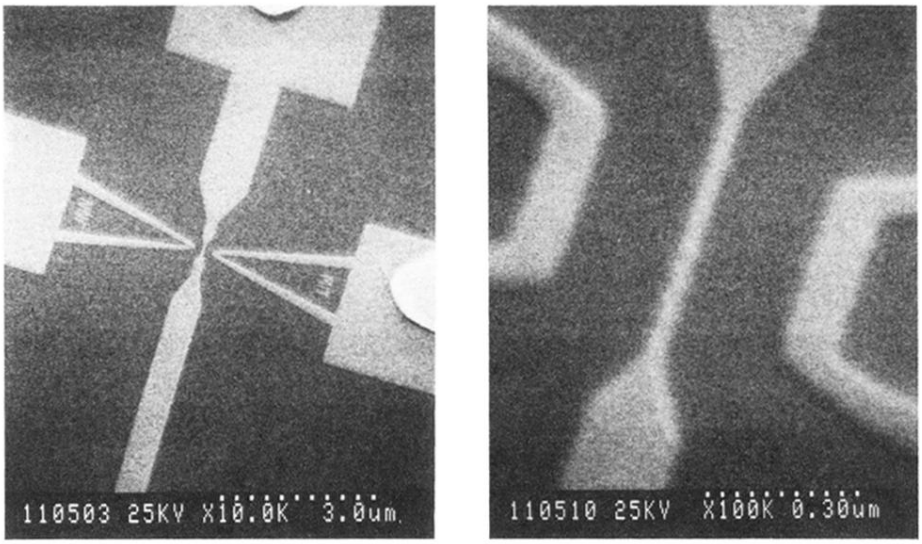


FIG. 7. SEM distant and close-up views of the split gates used to implement the leaky electron waveguide. The middle gate, which serves as the tunneling barrier for the channel, is 30 nm wide.